PHYSICAL REVIEW C **84**, 024313 (2011)

Development of collective structures over noncollective excitations in ^{139}Nd

S. Bhowal
Department of Physics, Surendranath Evening College, 24/2, M. G. Road, Kolkata 700009, India

G. Gangopadhyay
Department of Physics, University College of Science, University of Calcutta, 92 A. P. C. Road, Kolkata 700009, India

C. M. Petrache
Institut de Physique Nucléaire, Université Paris-Sud XI, CNRS/IN2P3 F-91406 Orsay, France

I. Ragnarsson
Division of Mathematical Physics, LTH, Lund University, P.O. Box 118, SE-221 00 Lund, Sweden

A. K. Singh
Department of Physics & Meteorology, Indian Institute of Technology, Kharagpur 721302, India

S. Bhattacharya
Saha Institute of Nuclear Physics, 1/AF Salt Lake, Kolkata 700064, India

H. Hübel, A. Neußer-Neffgen, A. Al-Khatib, P. Bringel, A. Bürger, N. Nenoff, and G. Schönwaßer
Helmholtz-Institut für Strahlen- und Kernphysik, Universität Bonn, Nußallee 14-16, D-53115 Bonn, Germany

G. B. Hagemann, B. Herskind, D. R. Jensen, and G. Sletten
Niels Bohr Institute, Blegdamsvej 17, DK-2100 Copenhagen, Denmark

P. Fallon and A. Görgen
Nuclear Science Division, Lawrence Berkeley National Laboratory, Berkeley, California 94720, USA

P. Bednarczyk and D. Curien
Institut de Recherches Subatomiques, 23 Rue du Loess, F-67037 Strasbourg, France

A. Korichi and A. Lopez-Martens
Centre de Spectrometrie Nucleaire et de Spectrometrie de Masse, F-91405 Orsay Campus, France

B. V. T. Rao and T. S. Reddy
Department of Nuclear Physics, Andhra University, Visakhapatnam 530003, India

Nirmal Singh
Department of Physics, Panjab University, Chandigarh 160014, India

(Received 23 March 2011; revised manuscript received 20 June 2011; published 17 August 2011)

High-spin states in ^{139}Nd were investigated using the reaction ^{96}Zr(^{48}Ca,5n) at a beam energy of 195 MeV and γ-ray coincidences were acquired with the Euroball spectrometer. Apart from several dipole bands at medium excitation energy, three quadrupole bands have been observed at high spin. Linking transitions connecting two of the high-spin bands to low-energy states have been observed. Calculations based on the cranked-Nilsson-Strutinsky formalism have been used to assign configurations for the high-spin quadrupole bands.

DOI: 10.1103/PhysRevC.84.024313 PACS number(s): 21.10.Re, 21.60.Ev, 23.20.Lv, 27.60.+j

I. INTRODUCTION

The nuclei around $Z = 64$ and $N = 82$ exhibit various excitation modes. At low energy they are expected to show single particle behavior because of the proximity of the shell closure. However, both protons and neutrons can occupy the intruder high-spin orbital $1h_{11/2}$, thus leading to moderately high spins at low energy. At higher energies multineutron excitations across the $N = 82$ shell gap give rise to high-spin bands based on triaxial deformation. Potential energy surface calculations exhibit a number of minima with different shapes, such as spherical or weakly deformed as well as deformed triaxial, oblate, or superdeformed shapes. The complex interplay of the variety of shapes with the single particle states gives rise to complicated and fascinating excitation spectra. The existence of different shapes has been confirmed experimentally by the observation of triaxial bands in ^{138,139,140}Nd [1,2], a highly deformed band in ^{138}Nd [3], and a superdeformed (SD) band in ^{140}Nd [4]. Another interesting feature in this region is the existence of low-deformation $M1$ bands arising from particle-hole excitations. Such bands have been observed in ^{137}Nd, [5] ^{139,143}Sm [6,7], $^{143-146}$Tb [8–11], and ^{142,144}Gd [12,13].

A few previous publications have focused on a detailed study of excited states in ^{139}Nd. Low-spin states up to 29/2 were studied by Gizon *et al.* [14] and Müller-Veggian *et al.* [15]. More recently, three additional studies on high-spin states were published. Petrache *et al.* [1] observed two triaxial high-spin bands using the reaction ^{96}Zr(^{48}Ca,5n) at an energy 195 MeV. The γ detection array consisted of 20 Ge detectors with anti-Compton shields and an inner ball of 71 BGO scintillator detectors. The spins of the bandheads were assumed to be around 49/2 and both sequences consisted of six $E2$ transitions in cascade. Recently, Kumar *et al.* [16] used the fusion evaporation reaction ^{128}Te(^{16}O,5n) to study the ^{139}Nd nucleus at a beam energy of 85 MeV. The detection set up consisted of 6 Compton-suppressed clover detectors with a 14-element NaI(Tl) multiplicity filter. The authors were able to deduce states up to an excitation energy of approximately 7 MeV and a spin up to 41/2. Xu *et al.* [17] used the same reaction at a beam energy of 90 MeV to populate states up to $47/2^-$ and nearly 8 MeV excitation energy using 14 Compton-suppressed Ge detectors.

In this article, we report on spectroscopy of high-spin states in ^{139}Nd using the Euroball detector array [18]. In the present work, the level scheme has been extended up to an energy of around 21 MeV and a spin of 89/2. The linking transitions between the lower-lying states and the two triaxial bands observed in the earlier work have been established resulting in a firm assignment of spin and parity to the bands. Several new bands have also been observed. The low-energy part of our scheme is nearly identical with that of Kumar *et al.* [16] with a few minor differences.

The details of the experimental setup are discussed in Sec. II. The results including the level scheme are presented in Sec. III. The most probable configurations of the different bands are discussed in Sec. IV on the basis of theoretical calculation using the cranked-Nilsson-Strutinsky (CNS) formalism for the high-spin quadrupole bands. Finally, the findings are summarized in Sec. V.

II. EXPERIMENTAL DETAILS

High-spin states in ^{139}Nd have been populated in the reaction ^{96}Zr(^{48}Ca,5n) with a 195 MeV Ca beam from the Vivitron tandem accelerator at IReS, Strasbourg. The target was a self-supporting ^{96}Zr foil of thickness 735 μg/cm^2. γ rays were studied with the Euroball spectrometer [18], consisting of 30 single, tapered Ge detectors, 15 cluster, and 26 clover composite Ge detectors, each surrounded by a BGO Compton-suppression shield. Out of the total number of 239 Ge crystals, 230 could be used in our analysis. Multiplicity information was obtained from the "inner ball" of 210 BGO detectors. Events were written to tape with the requirement that at least 11 BGO detectors of the inner ball and four Ge crystals before Compton suppression were in prompt coincidence. Presorting of the data, which included Compton suppression and addback for the composite detectors resulted in a total of 1.5×10^9 events with a γ-ray coincidence fold of $f \geqslant 3$. The γ-ray coincidences were sorted into coincidence arrays (cubes and hypercubes) and analysed using the RADWARE software package [19]. To determine the multipolarity of transitions, several gated matrices were sorted with all detectors on one axis and detectors at 90° and at forward/backward (f, b) angles, respectively, on the other axis. Gates were set on the axis with all detectors and the anisotropy ratio $R_\theta = I(\gamma_2^{fb}, \gamma_1^{\rm all})/I(\gamma_2^{90}, \gamma_1^{\rm all})$ was determined for the transitions in the resulting spectra. Alternatively, gated matrices were created with gates on stretched E2 transitions by sorting the events from detectors at forward and backward angles on one axis and those detected in detectors close to 90° on the other axis. The DCO ratios $R_{\rm DCO}$, for the γ rays were obtained by taking their intensity ratio at these two angles. Typical values of these ratios were 0.5 and 1.0 for γ rays of stretched dipole and quadrupole nature. Angular distribution measurements were not possible for several weak transitions. Thus, spin-parity values had to be inferred from systematics arguments for certain levels.

III. RESULTS AND LEVEL SCHEME

The level scheme of ^{139}Nd, developed in the present work, represents substantial improvement over the two recent spectroscopic studies reported by Kumar *et al.* [16] and Xu *et al.* [17]. We observe most of the transitions and cascades of the two previous studies. In addition, several new γ transitions have been identified and placed in the level scheme. The newly developed level scheme is presented in Figs. 1 and 2. The new features of the level scheme are discussed below. Results and level scheme, just before subsection A. Dipole bands: The experimental information on the observed transitions are given in Table I.

A. Dipole bands

An interesting feature of the level scheme at low energy is the presence of several $M1$ bands. Band A is a positive parity $M1$ band and is seen to start from the $21/2^+$ level at 2843.8 keV and continues up to the $27/2^+$ state. The set of transitions comprising this band was seen both in [16] and [17]. Based on intensity and coincidence arguments we have modified the ordering of the transitions. The 773 keV transition from the previously known $25/2^-$ level at 3840.1 keV in coincidence with the 224 keV transition and not with the 234 keV transition clearly points out the validity of our placement.

A negative-parity band B starts from a $27/2^-$ level at 3980.2 keV. It mixes strongly with the new band C which is based on a $31/2^-$ state. These bands continue up to states with spin-parity values of $41/2^-$ and $39/2^-$, respectively. Band B was observed both by Kumar *et al.* [16] and Xu *et al.* [17], though there are slight differences in the ordering of the transitions. All the γ transitions in band B (band (4) of Ref. [17]) placed earlier have been observed in the present work. However, based upon γ coincidence relationship, intensity analysis, and interband transitions between the bands

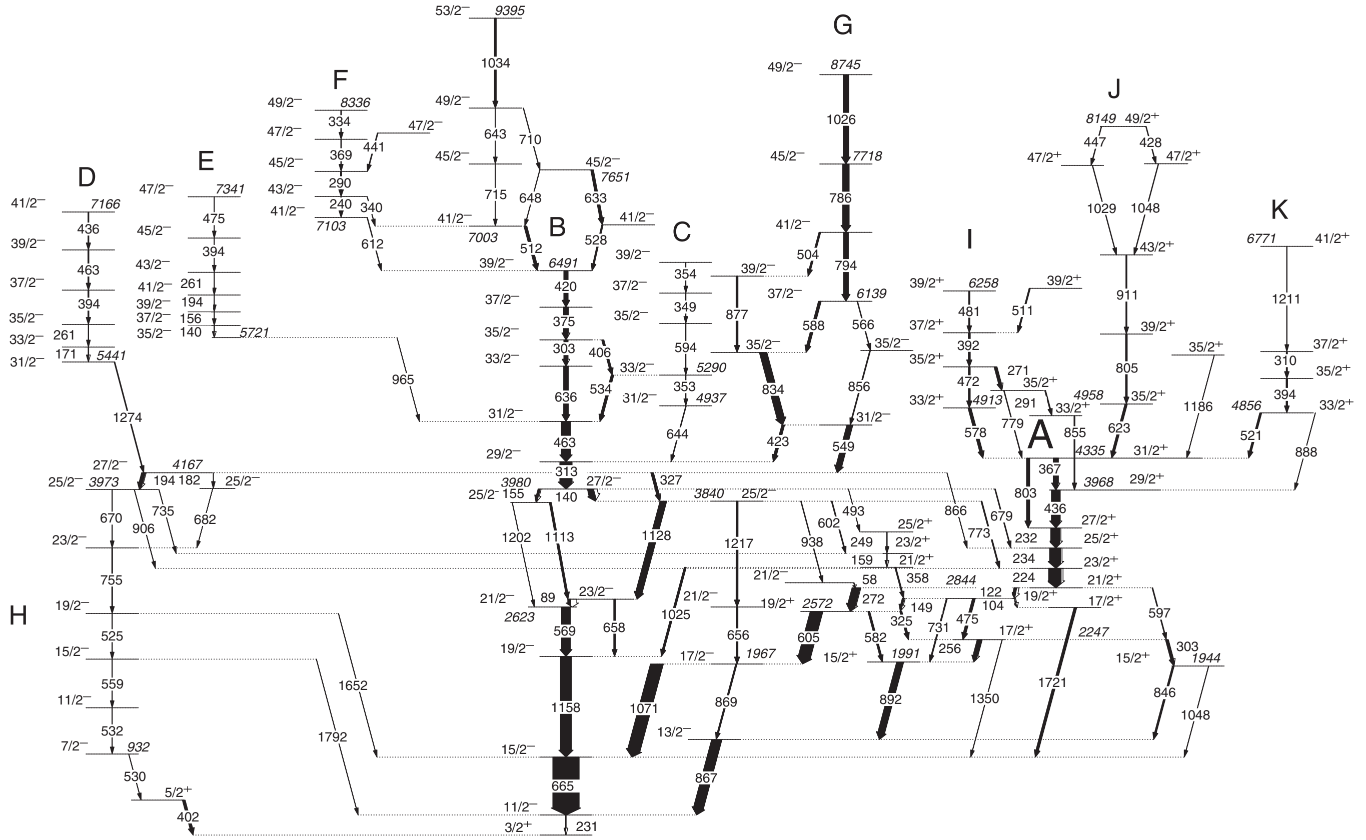

FIG. 1. Partial level scheme of ^{139}Nd. Energy values of levels important to our discussion have been shown only.

B and *C*, we have modified the sequence of γ transition as shown in Fig. 1. Xu *et al.* [17] have placed two 533 keV transitions, one from the 5285.3 keV ($33/2^-$) level (5290 keV in Fig. 1) and the other from the 6483.8 keV ($39/2^-$) level (6491 keV in Fig. 1), ultimately feeding band *B*. However, we could observe only the first one.

A cascade of four γ transitions with energies 353, 594, 349, and 354 keV forms the new band *C*. The band decays to band *B* through the 534 and 644 keV γ rays to the $31/2^-$ and $29/2^-$ states, respectively. The spin and parity of band *C* has been assigned on the basis of the measured DCO ratio compatible with a dipole character for the 534 and 644 keV transitions.

Band *D* is another *M*1 band comprising the transitions of energies 171, 261, 394, 463, and 436 keV. We have observed a decay transition of energy 1274 keV linking the band to the $27/2^-$ level at 4167.0 keV. The DCO ratio measured for this transition shows *E*2 character. Hence, we assign spin-parity $31/2^-$ to the level at 5441 keV. We have added one more transition with an energy of 436 keV on top of the band but we could not observe the 193.1 keV γ ray which was reported in [17].

A cascade of six dipole transitions, constituting band *E*, has been placed in the level scheme based on the observed decay of 965 keV transition from the bandhead at 5721.0 keV to the $31/2^-$ state of band *B*. The DCO ratio for the 965 keV transition is compatible with quadrupole multipolarity. Hence, spin and parity $35/2^-$ have been assigned to the level at 5721.0 keV.

Each of the two bands *D* and *E* have two transitions with energies 261 and 394 keV in common, but they are distinct. Xu *et al.* [17] reported a cascade of energies 193, 260, 393, and 462 keV. However, the 193 and the 463 keV γ ray actually belong to different bands.

We propose a modification in the placement of band *F* compared to the work by Xu *et al.* [17]. They did not observe the 612 keV transition below the 240 keV γ ray. We clearly see that the 512 keV transition is in coincidence with both the 290 and 340 keV γ rays but not with the 240 keV transition. We have also placed a γ ray of 334 keV on top of the band. Band *F* decays to band *B* through the linking transitions of 612 and 340 keV. Although angular distribution measurements for most of the transitions were not possible, we assume it to be an *M*1 band based on the similarity with other well established *M*1 bands.

In the present work we could observe all the transitions of band *G* placed by Xu *et al.* [17] and our intensity measurements and coincidence analysis also confirms the ordering. We have added one transition with 1026 keV above the 7718 keV($45/2^-$) level. The DCO analysis for the transitions confirms the spin assignments made in the previous work [17]. This band is linked to the deformed band 1 (see Figs. 1 and 2), through a number of connecting transitions.

Band *H* comprises the cascade of 402, 530, 532, 559, 525, and 755 keV γ rays. Apart from the last one these transitions are not observed in spectra gated by the 665, 1158, or 569 keV γ rays of the ground band. Therefore, we conclude that this cascade decays directly to the ground state. In addition, two decay-out transitions of energies 1652 and 1792 keV have

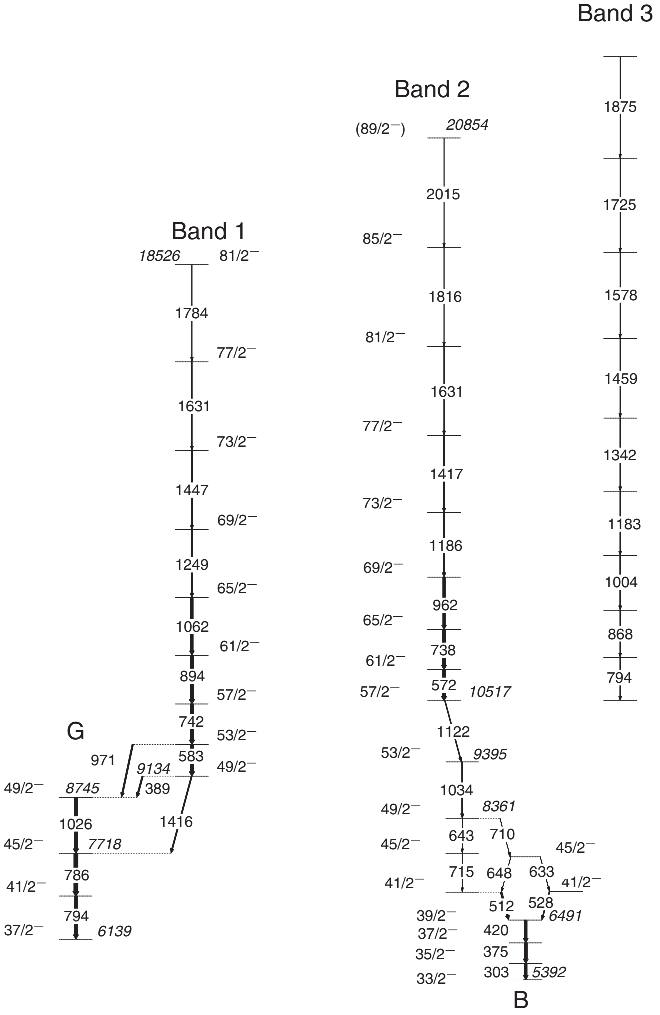

FIG. 2. High-energy bands in ^{139}Nd. Energy values of levels important to our discussion have been shown only.

been observed from band *H* to the ground band. The γ rays belonging to band *H* can be seen in spectra obtained by gating on other known γ transitions above the 3973 keV level. DCO measurements for the γ rays in band *H* have been found to be consistent with quadrupole multipolarity.

The sequence of γ transitions in band *I* was placed on the $31/2^+$ level at 4329 keV by Xu *et al.* [17] (4335 keV in Fig. 1). In the present work, the ordering of the transitions has been changed. Intensity measurements show that the 472 keV γ transition should be placed below both the 392 and 511 keV γ rays. This placement is further supported by the observed decay-out transitions of 271, 291, and 779 keV energies. We have also changed the placement of the 578 keV transition, which was placed parallel to the transitions of band *I* in the previous work [17]. We found that it is actually in coincidence with the band *I* transitions. There is a 481 keV transition parallel to the 511 keV γ ray. We did not observe the 309 keV γ ray in coincidence with the 578 keV transition. The energy and spin parity of the bandhead has also been modified.

We have added a new band consisting of quadrupole transitions (band *J*) in our scheme on top of the 4335 keV level $(31/2^+)$. DCO values measured for the transitions, except those of the top most level of the band, are compatible with quadrupole multipolarity extending the band up to $49/2^+$. Two decay paths consisting of two transitions each have been observed between the $49/2^+$ and the $43/2^+$ states.

The structure marked *K* was reported in the previous work [17]. We have added a 394 keV transition between the 521 and 310 keV transitions. We also observe a transition of 888 keV depopulating the $33/2^+$ state.

In addition, several new transitions feeding different bands have been added to the level scheme. These transitions have helped in assigning the spin parity to various levels. Negative parity was assigned to the levels at 1944, 1991, and 2246 keV in [17]. We propose that these levels have positive parity, since we observe a quadrupole transition of 582 keV between the $19/2^+$ state at 2572 keV and the level at 1991 keV. We expect it to be an *E*2 transition, thus changing the parity, of the 1991 keV level, and subsequently, of the levels at 1944 and 2246 keV.

In this work we did not observe the cascade of 1646.6, 167.9, 784.3, 953.8, and 406.5 keV transitions which was reported in the two earlier publications [16,17].

B. High-spin rotational bands

Two rotational bands, band 1 and 2, were observed by Petrache *et al.* [1] in an earlier experiment. However, the decay transitions to low-lying states could not be established and hence, spins and parities of the bands were not assigned. We confirm all the transitions placed in these two bands and have observed one new rotational sequence, band 3, at high spin in ^{139}Nd. Figures 3, 4, and 5 show gated spectra for the bands 1, 2, and 3, respectively.

In the present work, bands 1 and 2 have been extended up to $81/2^-$ and $89/2^-$, respectively. Connecting transitions linking bands 1 and 2 to low-lying states could be established. Band 1 is connected to band *G* via three decay-out transitions of energies 389, 1416, and 971 keV (see Fig. 2). The first two transitions connect the lowest level of band 1 to the $49/2^-$ and $45/2^-$ states of band *G*, respectively. The DCO ratio measured for the 389 and 1416 keV transitions show dipole and quadrupole character, respectively. Hence, spin-parity $49/2^-$ has been assigned to the lowest level of the band 1. The quadrupole character of the 971 keV decay transition, as evident from its DCO ratio, is in accordance with the spin and parity assignment to the depopulating levels. The multipolarities of the γ rays of band 1 have been found to be consistent with quadruple nature.

Band 2 decays through a cascade of transitions with 1122 and 1034 keV to the upper part of the dipole band *B*. The DCO ratios of both the transitions show their quadrupole character, most likely of electric nature. Hence, spin and parity of the lowest level of band 2 has been assigned as $57/2^-$. The 2015 keV transition at the top of the band is assumed to have a quadrupole character.

The decay-out transitions from band 3 could not be established and hence, spin and parity assignments to the states could not be established. However, DCO ratio measurements show that the band consists of transitions of quadrupole nature. The multipolarity of the 1875 keV transition at the top of the band could not be measured.

TABLE I. Energies, spin-parity assignments, intensities, DCO ratios, anisotropies, and multipolarities of γ-ray transitions of ^{139}Nd.

γ-ray energy E_γ (keV)	Initial state E_i (keV)	Final state E_f (keV)	J_i^π	→	J_f^π	Intensity I_γ	DCO ratio R_{DCO}	Anisotropy R_θ	Multipolarity
58.2	2902.0	2843.8	$21/2^-$	→	$21/2^+$	0.9		0.47	$E1$
89.1	2712.4	2623.3	$23/2^-$	→	$21/2^-$	11.6	0.42	0.38	$M1$
104.2	2721.4	2617.2	$19/2^+$	→	$17/2^+$	2.7	0.40	0.45	$M1$
122.4	2843.8	2721.4	$21/2^+$	→	$19/2^+$	10.6	0.48	0.44	$M1$
140.1	3980.2	3840.1	$27/2^-$	→	$25/2^-$	23.7	0.47	0.45	$M1$
140.0	5861.0	5721.0	$37/2^-$	→	$35/2^-$	1.1	0.37		$M1$
149.2	2721.4	2572.2	$19/2^+$	→	$19/2^+$	7.5	0.55		$M1$
155.2	3980.2	3825.0	$27/2^-$	→	$25/2^-$	8.2	0.47	0.56	$M1$
156.0	6017.0	5861.0	$39/2^-$	→	$37/2^-$	0.9	0.56	0.48	$M1$
159.1	3238.0	3078.9	$23/2^+$	→	$21/2^+$	1.4	0.48	0.50	$M1$
171.0	5612.0	5441.0	$33/2^-$	→	$31/2^-$	1.6		0.39	$M1$
182.0	4167.0	3985.0	$27/2^-$	→	$25/2^-$	0.51		0.57	$M1$
194.0	6211.0	6017.0	$41/2^-$	→	$39/2^-$	0.8			
194.2	4167.0	3973.0	$25/2^-$	→	$25/2^-$	13.8	0.52	0.51	$M1$
223.5	3067.3	2843.8	$23/2^+$	→	$21/2^+$	48.0	0.48	0.52	$M1$
231.0	231.0	0.0	$11/2^-$	→	$3/2^+$				$M4$
231.5	3532.4	3300.9	$27/2^+$	→	$25/2^+$	34.1	0.47	0.52	$M1$
233.6	3300.9	3067.3	$25/2^+$	→	$23/2^+$	42.0	0.48	0.51	$M1$
240.0	7343.0	7103.0	$43/2^-$	→	$41/2^-$	3.1	0.55	0.6	$M1$
249.0	3487.0	3238.0	$25/2^+$	→	$23/2^+$	1.8	0.62	0.61	$M1$
256.2	2246.8	1990.6	$17/2^+$	→	$15/2^+$	16.9	0.53	0.52	$M1$
261.0	5873.0	5612.0	$35/2^-$	→	$33/2^-$	1.12		0.41	$M1$
261.0	6472.0	6211.0	$43/2^-$	→	$41/2^-$				
271.0	5385.0	5114.0	$35/2^+$	→	$35/2^+$	6.9	0.5	0.51	$M1$
271.6	2843.8	2572.2	$21/2^+$	→	$19/2^+$	30.0	0.56	0.52	$M1$
290.0	7633.0	7343.0	$45/2^-$	→	$43/2^-$	4.1	0.55	0.55	$M1$
291.0	5114.0	4823.0	$35/2^+$	→	$33/2^+$	3.3	0.53	0.55	$M1$
302.7	2246.8	1944.1	$17/2^+$	→	$15/2^+$	10.2	0.53	0.56	$M1$
303.0	5695.4	5392.4	$35/2^-$	→	$33/2^-$	15.2	0.52	0.56	$M1$
309.7	5560.0	5250.3	$37/2^+$	→	$35/2^+$	4.1	0.53	0.51	$M1$
312.7	4292.9	3980.2	$29/2^-$	→	$27/2^-$	44.2	0.51	0.50	$M1$
325.4	2572.2	2246.8	$19/2^+$	→	$17/2^+$	7.5	0.56	0.42	$M1$
326.9	4167.0	3840.1	$27/2^-$	→	$25/2^-$	9.4	0.49	0.50	$M1$
334.0	8336.0	8002.0	$49/2^-$	→	$47/2^-$	2.5	0.47		$M1$
339.7	7343.0	7003.2	$43/2^-$	→	$41/2^-$	1.3	0.59	0.60	$M1$
349.0	6232.8	5883.8	$37/2^-$	→	$35/2^-$	1.21		0.42	$M1$
352.8	5289.8	4937.0	$33/2^-$	→	$31/2^-$	1.5	0.53		($M1$)
354.0	6586.8	6232.8	$39/2^-$	→	$37/2^-$	0.95			
357.5	3078.9	2721.4	$23/2^+$	→	$21/2^+$	4.1	0.6	0.55	$M1$
366.6	4335.0	3968.4	$31/2^+$	→	$29/2^+$	18.8	0.48	0.43	$M1$
369.0	8002.0	7633.0	$47/2^-$	→	$45/2^-$	2.1	0.58		$M1$
375.3	6070.7	5695.4	$37/2^-$	→	$35/2^-$	17.6	0.52	0.51	$M1$
388.6	9134.0	8745.0	$49/2^-$	→	$49/2^-$	8.1	0.53	0.57	$M1$
392.0	5777.0	5385.0	$37/2^+$	→	$35/2^+$	7.1	0.52	0.54	$M1$
394.1	6866.1	6472.0	$45/2^-$	→	$43/2^-$				
394.0	6267.0	5873.0	$37/2^-$	→	$35/2^-$	0.9	0.42		$M1$
394.3	5250.3	4856.0	$35/2^+$	→	$33/2^+$	5.2	0.53	0.52	$M1$
402.0	402.0	0.0	$5/2^+$	→	$3/2^+$	1.2	0.58		M1
405.6	5695.4	5289.8	$35/2^-$	→	$33/2^-$	8	0.51	0.53	$M1$
420.1	6490.8	6070.7	$39/2^-$	→	$37/2^-$	15.8	0.51	0.56	$M1$
423.4	4716.3	4292.9	$31/2^-$	→	$29/2^-$	11.5	0.48	0.46	$M1$
428.0	8149.0	7721.0	$49/2^+$	→	$47/2^+$	1.1	0.51		$M1$
436.0	3968.4	3532.4	$29/2^+$	→	$27/2^+$	33	0.52	0.55	$M1$
436.0	7166.0	6730.0	$41/2^-$	→	$39/2^-$	3.1		0.53	$M1$
441.0	8074.0	7633.0	$47/2^-$	→	$45/2^-$	2.6	0.52	0.55	$M1$
447.0	8149.0	7702.0	$49/2^+$	→	$47/2^+$	2.3	0.52	0.56	$M1$

TABLE I. (*Continued.*)

γ-ray energy E_γ (keV)	Initial state E_i (keV)	Final state E_f (keV)	J_i^π	→	J_f^π	Intensity I_γ	DCO ratio R_{DCO}	Anisotropy R_θ	Multipolarity
463.0	6730.0	6267.0	$39/2^-$	→	$37/2^-$	3.6		0.62	$M1$
463.3	4756.2	4292.9	$31/2^-$	→	$29/2^-$	34	0.52	0.51	$M1$
472.0	5385.0	4913.0	$35/2^+$	→	$33/2^+$	6.8	0.5	0.57	$M1$
474.6	2721.4	2246.8	$19/2^+$	→	$17/2^+$	20.0	0.53	0.57	$M1$
475.1	7341.2	6866.1	$47/2^-$	→	$45/2^-$	0.8	0.45		$M1$
481.0	6258.0	5777.0	$39/2^+$	→	$37/2^+$	4.4	0.68		$M1$
493.2	3980.2	3487.0	$27/2^-$	→	$25/2^+$				
504.0	6932.0	6428.1	$41/2^-$	→	$39/2^-$	6.5	0.52	0.54	$M1$
511.0	6288.0	5777.0	$39/2^+$	→	$37/2^+$	4.5	0.43	0.50	$M1$
512.4	7003.2	6490.8	$41/2^-$	→	$39/2^-$	10.6	0.52	0.52	$M1$
521.0	4856.0	4335.0	$33/2^+$	→	$31/2^+$	7.1	0.52	0.48	$M1$
525.0	2548.0	2023.0	$19/2^-$	→	$15/2^-$	1.3	1.03		$E2$
527.6	7018.4	6490.8	$41/2^-$	→	$39/2^-$	5.2	0.55	0.6	$M1$
530.0	932.0	402.0	$7/2^-$	→	$5/2^+$	1.0	0.73		$E1$
532.0	1464.0	932.0	$11/2^-$	→	$7/2^-$	1.0	0.82		$E2$
533.6	5289.8	4756.2	$33/2^-$	→	$31/2^-$	9.5	0.54	0.50	$M1$
549.3	4716.3	4167.0	$31/2^-$	→	$27/2^-$	22	1.03	0.98	$E2$
559.0	2023.0	1464.0	$15/2^-$	→	$11/2^-$	1.0	0.94		$E2$
566.4	6139.0	5572.6	$37/2^-$	→	$35/2^-$	2.2	0.56	0.48	$M1$
569.4	2623.3	2053.9	$21/2^-$	→	$19/2^-$	33	0.50	0.51	$M1$
572.1	11089.1	10517.0	$61/2^-$	→	$57/2^-$	18.6	0.83	1.18	$E2$
578.0	4913.0	4335.0	$33/2^+$	→	$31/2^+$	10.8	0.67	0.62	$M1$
581.6	2572.2	1990.6	$19/2^+$	→	$15/2^+$	7.1	0.88	0.93	$E2$
583.0	9717.0	9134.0	$53/2^-$	→	$49/2^-$	20.2	0.92		$E2$
588.3	6139.0	5550.7	$37/2^-$	→	$35/2^-$	18.8	0.56		$M1$
594.0	5883.8	5289.8	$35/2^-$	→	$33/2^-$	1.4	0.62		$M1$
597.0	2843.8	2246.8	$21/2^+$	→	$17/2^+$	2.8	0.82		$E2$
602.1	3840.1	3238.0	$25/2^-$	→	$23/2^+$	3.1	0.64	0.62	$E1$
604.9	2572.2	1967.3	$19/2^+$	→	$17/2^-$	47.0	0.66	0.69	$E1$
612.2	7103.0	6490.8	$41/2^-$	→	$39/2^-$	1.9	0.59		$M1$
622.6	4957.6	4335.0	$35/2^+$	→	$31/2^+$	8.7	0.85	0.83	$E2$
632.6	7651.0	7018.4	$45/2^-$	→	$41/2^-$	1.5	0.86	0.82	$E2$
636.2	5392.4	4756.2	$33/2^-$	→	$31/2^-$	17.6	0.52	0.54	$M1$
643.0	8361.0	7718.2	$49/2^-$	→	$45/2^-$	1.2	0.83		$E2$
644.1	4937.0	4292.9	$31/2^-$	→	$29/2^-$	2.3	0.67	0.59	$M1$
647.8	7651.0	7003.2	$45/2^-$	→	$41/2^-$	1.2	1.11		$E2$
656.0	2623.3	1967.3	$21/2^-$	→	$17/2^-$	6.6	1.01	0.82	$E2$
658.5	2712.4	2053.9	$23/2^-$	→	$19/2^-$	6.2	0.82	0.83	$E2$
665.4	896.4	231.0	$15/2^-$	→	$11/2^-$	100	1.02	1.13	$E2$
670.0	3973.0	3303.0	$25/2^-$	→	$23/2^-$	0.85	0.61		$M1$
679.2	3980.2	3300.9	$27/2^-$	→	$25/2^+$	2.7	0.7	0.71	$E1$
682.0	3985.0	3303.0	$25/2^-$	→	$23/2^-$	0.34			
710.0	8361.0	7651.0	$49/2^-$	→	$45/2^-$	1.5	0.84		$E2$
714.7	7718.2	7003.2	$45/2^-$	→	$41/2^-$	1.3	0.81		$E2$
730.8	2721.4	1990.6	$19/2^+$	→	$15/2^+$	3.8	0.8		$E2$
735.0	3973.0	3238.0	$25/2^-$	→	$23/2^+$				
738.0	11827.1	11089.1	$65/2^-$	→	$61/2^-$	17.8	0.95	0.87	$E2$
742.0	10459.0	9717.0	$57/2^-$	→	$53/2^-$	20.1	0.88		$E2$
755.0	3303.0	2548.0	$23/2^-$	→	$19/2^-$	2.8	1.02	0.9	$E2$
772.8	3840.1	3067.3	$25/2^-$	→	$23/2^+$	3.8	0.77	0.75	$E1$
779.0	5114.0	4335.0	$35/2^+$	→	$31/2^+$	2.1	0.89	0.95	$E2$
786.2	7718.2	6932.0	$45/2^-$	→	$41/2^-$	24.6	0.93	1.00	$E2$
793.6	6932.0	6139.0	$41/2^-$	→	$37/2^-$	18.6	1.03	0.93	$E2$
794.0	$x + 794$	x	$J + 2$	→	J	3.9	1.03	0.92	$E2$
802.6	4335.0	3532.4	$31/2^+$	→	$27/2^+$	12.1	0.85	0.86	$E2$
804.6	5762.2	4957.6	$39/2^+$	→	$35/2^+$	6.1	0.96	0.87	$E2$

TABLE I. (*Continued.*)

γ-ray energy E_γ (keV)	Initial state E_i (keV)	Final state E_f (keV)	J_i^π	$\rightarrow$	J_f^π	Intensity I_γ	DCO ratio R_{DCO}	Anisotropy R_θ	Multipolarity
834.4	5550.7	4716.3	$35/2^-$	$\rightarrow$	$31/2^-$	28.0	0.91	0.89	$E2$
845.9	1944.1	1098.2	$15/2^+$	$\rightarrow$	$13/2^-$	6.4	0.61		$E1$
854.6	4823.0	3968.4	$33/2^+$	$\rightarrow$	$29/2^+$	3.5	0.83	0.79	$E2$
856.3	5572.6	4716.3	$35/2^-$	$\rightarrow$	$31/2^-$	3.1	0.86		$E2$
866.1	4167.0	3300.9	$27/2^-$	$\rightarrow$	$25/2^+$	0.74			$E1$
867.2	1098.2	231.0	$13/2^-$	$\rightarrow$	$11/2^-$	38.1	0.59	0.55	$M1$
868.0	$x+1662$	$x+794$	$J+4$	$\rightarrow$	$J+2$	3.7	0.93	0.96	$E2$
869.1	1967.3	1098.2	$17/2^-$	$\rightarrow$	$13/2^-$	5.1	1.08	1.0	$E2$
877.4	6428.1	5550.7	$39/2^-$	$\rightarrow$	$35/2^-$	7	1.05	0.93	$E2$
887.6	4856.0	3968.4	$33/2^+$	$\rightarrow$	$29/2^+$	0.8	0.89	0.93	$E2$
892.4	1990.6	1098.2	$15/2^+$	$\rightarrow$	$13/2^-$	26.1	0.77		$E1$
894.0	11353.0	10459.0	$61/2^-$	$\rightarrow$	$57/2^-$	19.1	0.89	1.08	$E2$
905.7	3973.0	3067.3	$25/2^-$	$\rightarrow$	$23/2^+$				
910.8	6673.0	5762.2	$43/2^+$	$\rightarrow$	$39/2^+$	3.8	1.15	0.91	$E2$
938.1	3840.1	2902.0	$25/2^-$	$\rightarrow$	$21/2^-$	2.1	0.89	0.87	$E2$
961.9	12789.0	11827.1	$69/2^-$	$\rightarrow$	$65/2^-$	15.6	0.99	1.09	$E2$
964.8	5721.0	4756.2	$35/2^-$	$\rightarrow$	$31/2^-$	0.8		0.84	$E2$
971.4	9716.6	8745.0	$53/2^-$	$\rightarrow$	$49/2^-$	8.5	0.96	0.87	$E2$
1004.0	$x+2666$	$x+1662$	J + 6	$\rightarrow$	J + 4	4.7	0.87	0.91	$E2$
1025.0	3078.9	2053.9	$21/2^+$	$\rightarrow$	$19/2^-$	7.3	0.58		$E1$
1026.4	8745.0	7718.2	$49/2^-$	$\rightarrow$	$45/2^-$	20.1	1.1	0.96	$E2$
1029.0	7702.0	6673.0	$47/2^+$	$\rightarrow$	$43/2^+$	1.7		1.1	$E2$
1034.0	9395.0	8361.0	$53/2^-$	$\rightarrow$	$49/2^-$	6.8	1.02	0.95	$E2$
1047.7	1944.1	896.4	$15/2^+$	$\rightarrow$	$15/2^-$	1.1	0.78		$E1$
1048.0	7721.0	6673.0	$47/2^+$	$\rightarrow$	$43/2^+$	1.8	0.99		$E2$
1061.5	12415.0	11353.0	$65/2^-$	$\rightarrow$	$61/2^-$	15.5	0.97	1.10	$E2$
1070.9	1967.3	896.4	$17/2^-$	$\rightarrow$	$15/2^-$	47.8	0.52	0.46	$M1$
1112.6	3825.0	2712.4	$25/2^-$	$\rightarrow$	$23/2^-$	7.7	0.59	0.59	$M1$
1122.0	10517.0	9395.0	$57/2^-$	$\rightarrow$	$53/2^-$	5.7	0.92	0.94	$E2$
1127.7	3840.1	2712.4	$25/2^-$	$\rightarrow$	$23/2^-$	24.4	0.49	0.41	$M1$
1157.5	2053.9	896.4	$19/2^-$	$\rightarrow$	$15/2^-$	41.7	1.05	1.03	$E2$
1183.0	$x+3849$	$x+2666$	$J+8$	$\rightarrow$	$J+6$	3.6	1.02	0.97	$E2$
1186.2	13975.2	12789.0	$73/2^-$	$\rightarrow$	$69/2^-$	9.6	1.17	1.20	$E2$
1186.0	5521.0	4335.0	$35/2^+$	$\rightarrow$	$31/2^+$	0.9		1.01	$E2$
1201.7	3824.6	2623.3	$25/2^-$	$\rightarrow$	$21/2^-$	1	1.03	1.01	$E2$
1211.0	6771.0	5560.0	$41/2^+$	$\rightarrow$	$37/2^+$	1.5	0.97		$E2$
1216.8	3840.1	2623.3	$25/2^-$	$\rightarrow$	$21/2^-$	7.1	1.03	1.07	$E2$
1248.8	13663.8	12415.0	$69/2^-$	$\rightarrow$	$65/2^-$	9.5	1.06	1.18	$E2$
1274.0	5441.0	4167.0	$31/2^-$	$\rightarrow$	$27/2^-$	2.81		0.86	$E2$
1342.0	$x+5191$	$x+3849$	$J+10$	$\rightarrow$	$J+8$	3.5	1.04		$E2$
1350.4	2246.8	896.4	$17/2^+$	$\rightarrow$	$15/2^-$	1.2	0.8		$E1$
1415.8	9134.0	7718.2	$49/2^-$	$\rightarrow$	$45/2^-$	6.9	1.01		$E2$
1416.9	15392.1	13975.2	$77/2^-$	$\rightarrow$	$73/2^-$	6.9	1.05	1.07	$E2$
1447.2	15111.0	13663.8	$73/2^-$	$\rightarrow$	$69/2^-$	7.2	1.11		$E2$
1459.0	$x+6650$	$x+5191$	$J+12$	$\rightarrow$	$J+10$	2.3	1.07	1.12	$E2$
1578.0	$x+8228$	$x+6650$	$J+14$	$\rightarrow$	$J+12$	1.5	1.26		$E2$
1631.0	16742.0	15111.0	$77/2^-$	$\rightarrow$	$73/2^-$	4.0	1.08	1.07	$E2$
1631.0	17023.0	15392.1	$81/2^-$	$\rightarrow$	$77/2^-$	3.5	1.02		$E2$
1651.6	2548.0	896.4	$19/2^-$	$\rightarrow$	$15/2^-$				
1720.8	2617.2	896.4	$17/2^+$	$\rightarrow$	$15/2^-$	9.7	0.74		$E1$
1725.0	$x+9953$	$x+8228$	$J+16$	$\rightarrow$	$J+14$	1.1		1.19	$E2$
1784.0	18526.0	16742.0	$81/2^-$	$\rightarrow$	$77/2^-$	2.2		1.15	$E2$
1792.0	2023.0	231.0	$15/2^-$	$\rightarrow$	$11/2^-$				
1816.0	18839.0	17023.0	$85/2^-$	$\rightarrow$	$81/2^-$	2.1	1.07		$E2$
1875.0	$x+11828$	$x+9953$	$(J+18)$	$\rightarrow$	$J+16$				
2015.0	20854.0	18839.0	$(89/2^-)$	$\rightarrow$	$85/2^-$	1.3			

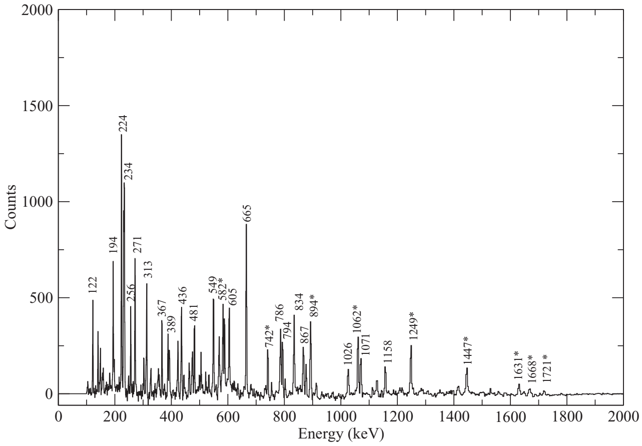

FIG. 3. Triple-gated sum spectrum for band 1 in ^{139}Nd. The gates were set on all transitions of the band. The transitions marked with asterisks represent the members of the band.

IV. DISCUSSION

The nucleus ^{139}Nd has 60 protons and 79 neutrons. The low-energy structure can be considered to arise from an interaction between 10 proton particles and three neutron holes in the $Z = 50$ and $N = 82$ shells, respectively. High-energy excitations involve neutron excitation across the shell gap. In the low-energy regime, the nucleus is expected to have a small deformation $\beta \sim 0.1$. Thus it is convenient to express the single particle states in terms of j-shell quantum numbers. Here, obviously neutrons are holes and protons in the $h_{11/2}$ subshell are particles. However, the $\pi g_{7/2}$ and $\pi d_{5/2}$ states interact strongly and may be considered as a mixture of hole and particle states.

A. Discussion of the low-spin bands

The level scheme of ^{139}Nd presents a very complex structure at low and medium spins. We have arranged some of the states in sequences of transitions such that they resemble bands structures, but we are aware that this choice is somewhat arbitrary.

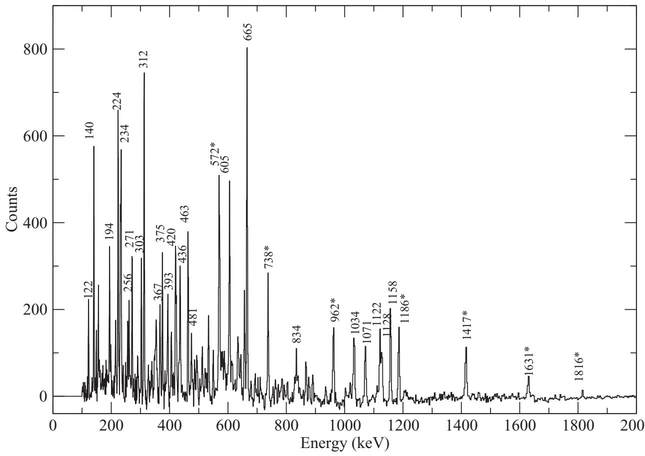

FIG. 4. Triple-gated sum spectrum for band 2 ^{139}Nd. The gates were set on all transitions of the band. The transitions marked with asterisks represent the members of the band.

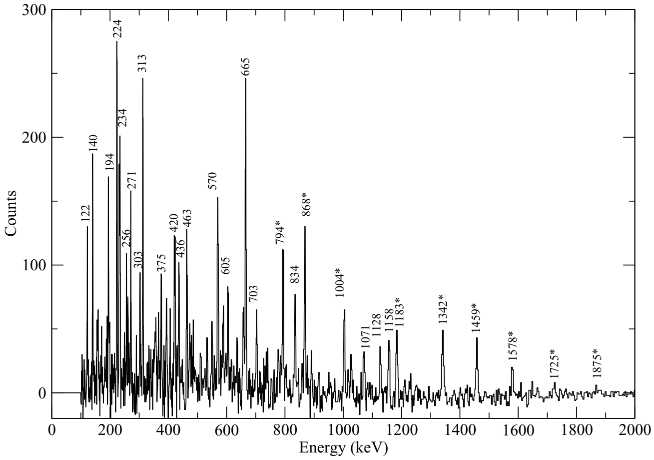

FIG. 5. Triple-gated sum spectrum for band 3 in ^{139}Nd. The gates were set on all transitions of the band. The transitions marked with asterisks represent the members of the band.

We will not discuss here all the observed states at low spin, since many of them have been observed and discussed recently employing the tilted axis cranking model [16] and triaxial plus particle rotor model [17]. We will only briefly discuss the possible configurations of the newly observed structures.

The ground state has $J^\pi = 3/2^+$ which is a one-quasiparticle state with the odd neutron hole in the $2\nu d_{3/2}$ orbital. The first excited state with $J^\pi = 11/2^-$ is isomeric with a half-life of 5.5 h [20]. It results from a hole in the $1\nu h_{11/2}$ orbital. The higher lying levels are compared to the low-energy states in the neighboring even-even core, ^{140}Nd, in Fig. 6. The levels in ^{139}Nd have been plotted relative to the $11/2^-$ state. The agreement between the two level schemes establishes the structure of these states in ^{139}Nd.

The weakly populated negative-parity cascade called H is most probably based on the $\nu f_{7/2}$ orbital. It decays to the $5/2^+$ state which could have a $\nu g_{7/2}$ configuration, but also to the band built on the $\nu h_{11/2}$ isomer through two high-energy $E2$ transitions. This structure is interesting since it gives the first evidence in this mass region of the presence close to the Fermi level of the $\nu f_{7/2}$ quasiparticle orbital from above the $N = 82$ shell closure, which can interact with the $\nu h_{11/2}$ orbital and induce the observed irregularities in the nonyrast states of the $\nu h_{11/2}$ band: the $13/2^-$ state lies above the $15/2^-$ state, while the $17/2^-$ state is found below the $19/2^-$ state.

An isomer above the $19/2^+$ level at 2572.2 keV has been observed with a lifetime of 272 ± 4 ns in the work of Ferraton *et al.* [21]. Recent data from an experiment at Jyväskylä, in which a combination of the Jurogam array and RITU [22] along with a Ge array at the focal plane, show prompt-delayed coincidences and establish the transitions populating the $23/2^+$ isomer, which lies 45 keV above the $19/2^+$ state [23]. The $23/2^+$ isomer is populated by three $E1$ transitions from three $25/2^-$ states (not shown in Fig. 1). The configuration of the $23/2^+$ isomer is $\nu[(h_{11/2})^{-2}(d_{3/2})^{-1}]$. Therefore, the configurations of the three $25/2^-$ states most likely involve the same neutron configuration of the $23/2^+$ isomer and two more nucleons from a broken pair, most likely protons in the $\pi h_{11/2}$ and $\pi g_{7/2}$ orbitals. The choice of protons

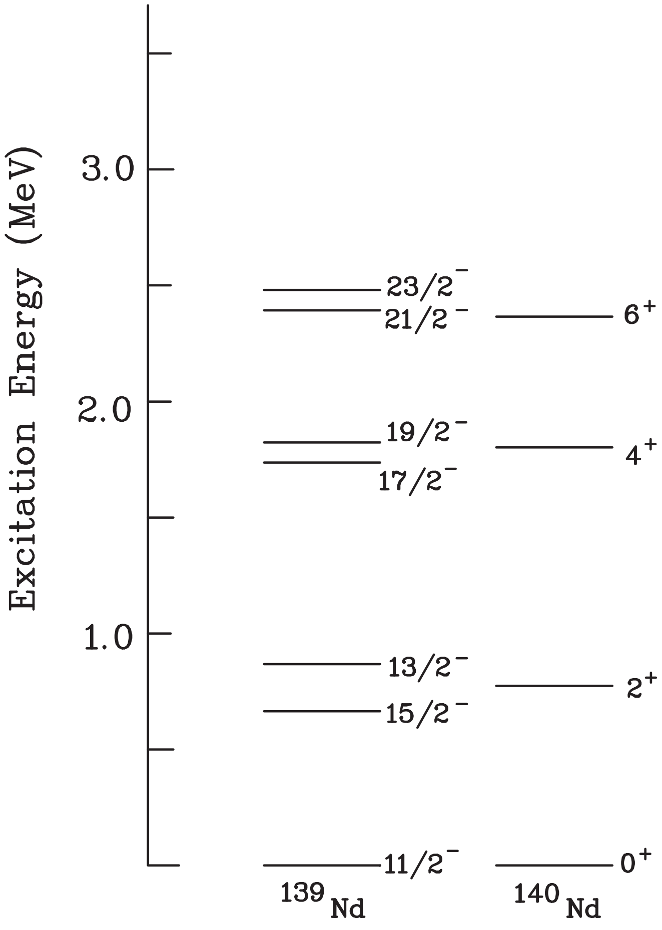

FIG. 6. States in ^{139}Nd obtained by coupling of a quasihole in $1\nu h_{11/2}$ orbital to the core states in ^{140}Nd. The corresponding core states are also shown. See text for details.

is preferred since the $25/2^-$ states also decay to the $21/2^-$ and $23/2^-$ members of the $\nu h_{11/2}$ band, which originate from the $\nu h_{11/2} \otimes 6^+$ multiplet, in which the 6^+ state has a $\pi(d_{5/2}g_{7/2})$ configuration.

The two $27/2^-$ states decaying to the $25/2^-$ levels most probably have the same configuration as the $25/2^-$ states. This suggests that the configuration of the strongly populated band *B* and of the weaker band *C* with which it interacts involves five quasiparticles, three neutrons and two protons: $\nu[(h_{11/2})^{-2}(d_{3/2})^{-1}] \otimes \pi(d_{5/2}g_{7/2})$.

There are four more cascades, called *D*, *I*, *J*, and *K*, which start at spins around $31/2 - 33/2$, and decay to states with assigned three quasiparticle configuration. They can be built on configurations involving five quasiparticles.

The bands *E* and *F* start at higher spins, $35/2^-$ and $41/2^-$, respectively. Their configurations should involve a larger number of quasiparticles than in the bands starting at lower spins, and therefore we believe that these bands have seven quasiparticle configurations.

B. Discussion of the high-spin rotational bands

The high-spin level scheme of ^{139}Nd is dominated by deformed collective bands consisting of *E*2 transitions. These bands are regular in structure and have nearly constant dynamic moments of inertia around 20 $\hbar^2$MeV^{-1} (see Fig. 7), which are much smaller than those observed in lighter Nd isotopes [24] and a recently observed SD band in ^{140}Nd [4]. This indicates a smaller deformation of the bands observed in ^{139}Nd, which is similar to several such bands observed in the neighboring ^{140}Nd nucleus [2]. These low deformation bands have been interpreted as triaxial structures [1]. Potential energy surface (PES) calculations show the existence of local minima corresponding to triaxial shape with $\varepsilon_2 = 0.20 - 0.30$, $\gamma = 30^\circ - 40^\circ$ [2].

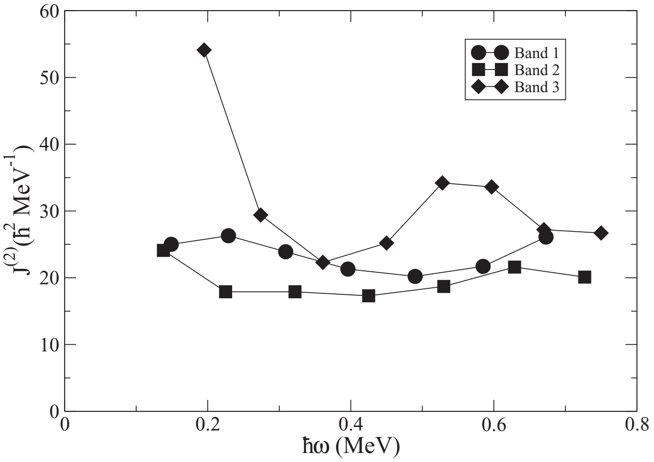

FIG. 7. Dynamic moment of inertia for the collective bands in ^{139}Nd.

The cranked-Nilsson-Strutinsky formalism [25,26] has been used to describe the triaxial high-spin rotational bands in ^{138,139}Nd [1] and ^{140}Nd [2]. This model has been successful in explaining high-spin bands in different mass regions, including terminating bands in mass 60, 110, and 150 regions [26], and superdeformed bands, for example, in the $A = 130$ [27] and $A = 150$ [28] regions. Even though the pairing is neglected, the calculated bands should reproduce well the observed bands, since we are dealing with very high spin states in which the pairing is expected to be strongly reduced. Configurations are assigned by the number of nucleons in orbitals which have their main amplitudes in different *j* shells or groups of *j* shells. In $A \approx 140$ nuclei, the configurations are given relative to the ^{132}Sn ($Z = 50$, $N = 82$) core by the shorthand notation $[p_1, n_1(n_2 n_3)]$, representing p_1 protons in $h_{11/2}$ orbitals, n_1 neutron holes in $h_{11/2}$, n_2 neutrons in $(h_{9/2}f_{7/2})$, and n_3 neutrons in $i_{13/2}$. An important development since the calculations on $^{138-140}$Nd were published [1,2] is that the formalism now includes the possibility to calculate the absolute energy of a high-spin state [29]. Thus, the observed energy based on the mass of the ground state and the excitation energy relative to the ground state can be compared with calculations.

The results of the CNS calculations are presented in Fig. 8, where calculated $(E - E_{\mathrm{RLD}})$ curves corresponding to low-lying configurations in the triaxial minimum are drawn as a function of spin. As one can see, there is a high density of bands all having a pronounced curvature (corresponding

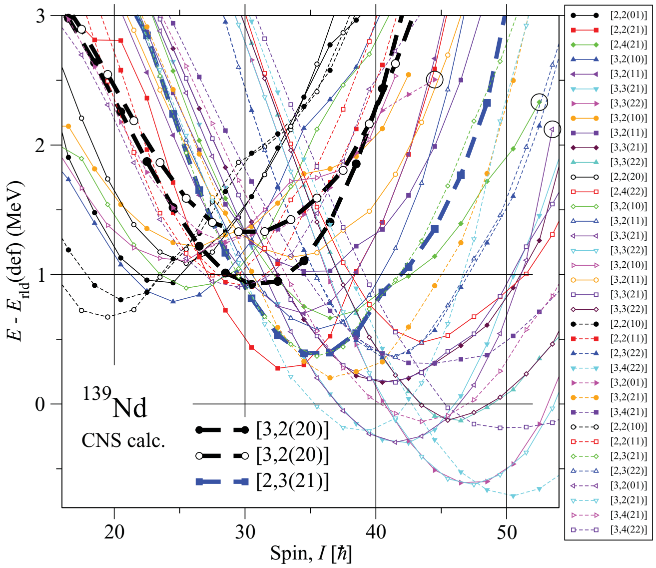

FIG. 8. (Color online) Calculated configurations relative to a rotating liquid drop reference for the triaxial high-spin bands in ^{139}Nd. Solid and dashed lines are used for positive and negative parity configurations, respectively. Closed symbols are used for signature $\alpha = 1/2$ and open symbols for signature $\alpha = -1/2$. The thick lines and large symbols are used to draw the configurations of our preferred assignments for the high-spin bands in ^{139}Nd. The shapes of the curves are relatively insensitive to the single-particle parameters while absolute energies of the different bands are much more sensitive to the parameters, that is, to the position of the different j shells. Therefore, it is not really a problem that with present parameters, the configurations which are tentatively assigned to the observed bands are calculated a few hundred kilo-electron-volts above yrast.

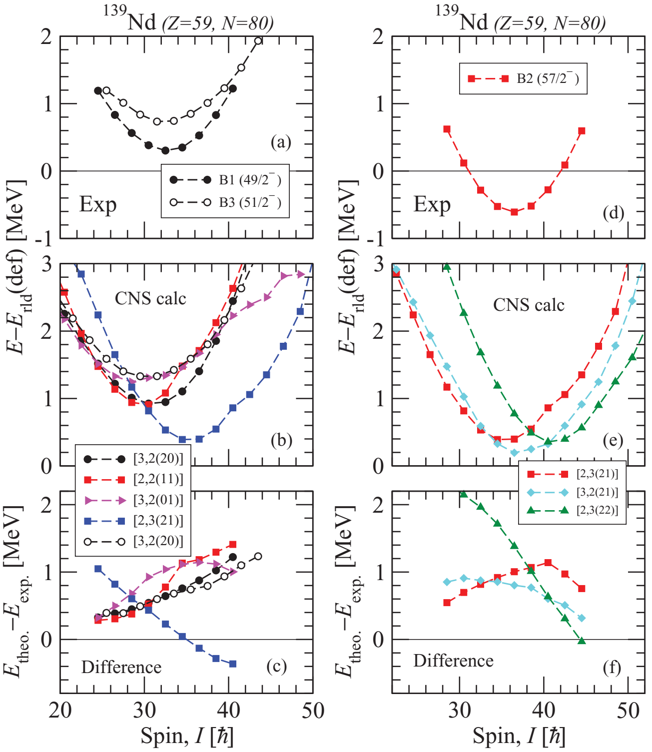

FIG. 9. (Color online) Comparison between the experimental (upper panels) and theoretical (middle panels) excitation energy relative to a rotating liquid drop reference and their differences (lower panels) for the high-spin bands in ^{139}Nd. Bands 1 and 2 are compared with several calculated configurations in the left and right panels, respectively. Furthermore, a possible assignment of band 3 as a signature partner of band 1 is illustrated in the left panels. Solid and dashed lines and closed and open symbols are used as in Fig. 8. Symbols and colors are used as defined in the legends for the calculated configurations in the middle panels and for their comparison with the observed bands in the lower panels. The same symbols and colors are used for the experimental bands and our preferred assignment.

to a small $\mathcal{J}^{(2)}$ moment of inertia) which is a fingerprint of triaxial shape. The calculated minima occur at spin values which increase with the number of occupied high-j orbitals. Because of the uncertainties in the single-particle parameters, the relative energies are uncertain to $0.5 - 1.0$ MeV. On the other hand, one should also note that a change of the single-particle parameters will mainly affect the excitation energy of the different configurations while other properties like the curvature and the position of the minima are more or less unaffected.

The large number of configurations in the yrast region on Fig. 8 suggests that it might be very difficult to assign configurations to the observed bands. However, if the parity and signature is measured, the number of possible configurations is highly reduced as illustrated for band 1 and band 2 in Fig. 9. In any case, we can mainly conclude that the general agreement between calculations and experiment gives very strong evidence that the collective high-spin bands in ^{139}Nd and neighboring isotopes are formed by configurations at triaxial shape. These configurations have 2 or 3 high-j $h_{11/2}$ protons, with one or several neutrons excited across the $N = 82$ gap into the high-j $h_{9/2}f_{7/2}$ and $i_{13/2}$ subshells. These configurations can be characterized for example by the maximum spin contribution from the high-j particles, $I^h_{\rm max}$. The value of $I^h_{\rm max}$ makes it possible to get a general idea about possible configuration assignments for an observed band because it is strongly correlated to the spin value at the minimum when the energies of the rotational bands are plotted relative to the rotating liquid drop reference, see Fig. 8 of Ref. [2]. This puts a strong constraint on possible assignments for the different observed bands if their spin and excitation energies are known and it becomes interesting to investigate if it is possible to give a more detailed configuration assignment to these bands.

The previous calculations on ^{139}Nd [1] suggested the [2,2(21)], [3,2(20)], or [2,2(11)] configurations as the most probable assignment for band 1 if the spin value which has now been confirmed, 49/2 was assigned to the lowest observed level. Now, since parity has been measured as negative, the [2,2(21)] configuration can be excluded. On the other hand, also the [3,2(01)] configuration has its minimum in the $E - E_{\rm RLD}$ curve at $I \approx 30$ so it is another possible assignment for band 1. As seen in Fig. 9(c), the difference between calculations and experiment is positive for the three

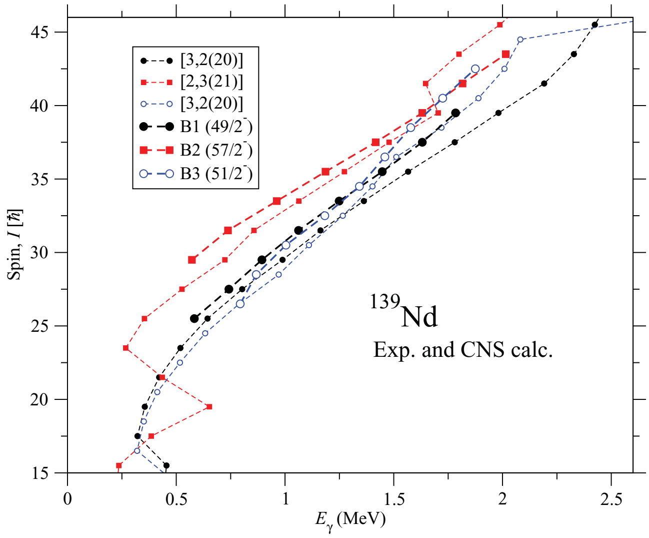

FIG. 10. (Color online) Spin vs transition energy for the high-spin bands in ^{139}Nd and for the calculated configurations which are tentatively assigned to them.

suggested assignments but it falls roughly within the expected range of ±1 MeV [29]. On the other hand, the increase of the differences with increasing spin (the slope) is somewhat larger than in other regions where the CNS model has been applied [29]. It reflects the fact that the total alignment is larger in experiment than in calculations as seen more clearly in Fig. 10 for our preferred assignment, [3,2(20)]. In order to illustrate the importance of the slope in the differences between calculations and experiment, we have added a forth configuration, [2,3(21)], in Fig. 9(b) which has its minimum at a too large spin value ($I \approx 36$) leading to a large down slope in Fig. 9(c).

The spin of the lowest observed level in band 2 was estimated to be 49/2 in Ref. [1], a value much smaller than the spin-parity $57/2^-$ assigned to band 2 from the present results. The experimental band is shown relative to the rotating liquid drop energy in Fig. 9(d). It is compared with the calculated bands with $(\pi, \alpha) = (-, +1/2)$ from Fig. 8 which have their minima at $I \approx 36$, [2,3(21)] and [3,2(21)]. Our preferred configuration for band 2 (see below the discussion of the spin alignments of the bands) is [2,3(21)], that is,

$$\pi(d_{5/2}g_{7/2})^8(h_{11/2})^2\nu(d_{3/2}s_{1/2})_-^{-3}(h_{11/2})_+^{-3}(h_{9/2}f_{7/2})^2(i_{13/2})_+^1.$$

In addition, to give an idea of the difference between our preferred configurations and the neighboring candidate configurations, the [2,3(22)] band is also shown to illustrate the strong down slope of the difference in this case where the minimum in Fig. 8(e) is calculated just above $I = 40$.

When assigning a spin value to band 3, one important input is the difference between the largest and smallest energy when the band is drawn relative to the rotating liquid drop reference. If this difference is much larger than 1 MeV, it indicates that the highest energy state is at an unrealistic high-excitation energy and therefore would be difficult to observe. One possible choice for the lowest energy state estimated from the analysis of the decay out of the band is the 51/2 value used in Fig. 9(a), with an increase in spin by $1\hbar$ or $2\hbar$ as possible alternatives. We have then chosen the 51/2 value because the band will then fit nicely as the signature partner of band 1 if these two bands are assigned as [3,2(20)]

$$\pi(d_{5/2}g_{7/2})_{\mp}^{7}(h_{11/2})_-^3\nu(d_{3/2}s_{1/2})_-^{-3}(h_{11/2})^{-2}(h_{9/2}f_{7/2})^2,$$

where the signature of an odd number of particles are given as subscript + and − for $\alpha = +1/2$ and $\alpha = -1/2$, respectively.

With our preferred assignments, the differences between the observed and calculated energies drawn in the lower panel of Fig. 9 are almost the same for all three bands. This shows that the relative properties of the bands are reproduced in the calculations. One observation is that the irregularity at $I \approx 40$ in the calculated [2,3(21)] band is not observed in band 2. This irregularity is caused by a crossing within the $N = 4$ proton orbitals. It is not a serious problem because the observed band 2 could as well follow the diabatic path through the crossing and one could also note that the crossing would be calculated at different spin values if the spacing between the proton $d_{5/2}$ and $g_{7/2}$ subshells were different.

The agreement between calculations and experiment for our preferred assignment is also illustrated by the spin versus transition energy curves shown in Fig. 10. The fact that the average slope is essentially the same in experiment and calculations shows that the $\mathcal{J}^{(2)}$ moment of inertia is reproduced. This can also be deduced from the similar curvatures in Fig. 9. Note especially that the slope of experimental band 3 is larger than that of band 1, and that the slope difference is well reproduced by the two signatures of the [3,2(20)] configuration. This behavior can also be deduced from the smaller curvature for the unfavored signature in Fig. 9. It is natural to define the aligned spin as the crossing with the $E_\gamma = 0$ axis if the "lines" in Fig. 10 are extrapolated to $E_\gamma = 0$. This value falls in the approximate range $18 - 24\hbar$ and can be correlated to the maximum spin contribution from the high-j particles or to the spin value of the minima in Fig. 9 as discussed in Ref. [2].

V. SUMMARY

High-spin states in ^{139}Nd have been populated in the reaction ^{96}Zr(^{48}Ca,5n) at a beam energy of 195 MeV. The Euroball spectrometer was used to detect the γ-ray coincidences. The level scheme was extended considerably and most of the existing information was confirmed. A number of dipole bands have been placed in the level scheme and one new quadrupole band has been observed at high spin and excitation energy. Transitions linking two previously known high-spin bands to the lower states have been found and the spin parity of these states thereby determined.

The high-spin quadrupole bands have been interpreted using the cranked-Nilsson-Strutinsky formalism. The comparison between calculations and experiment give strong evidence that these bands are formed in configurations at triaxial shape, $\varepsilon_2 = 0.20 - 0.30$, $\gamma = 30°$-$40°$, with approximately five high-j particles distributed over 11/2, $\nu h_{9/2}f_{7/2}$ and $\nu i_{13/2}$ subshells, while more detailed configuration assignments become uncertain. Future high-statistics experiments allowing to link more bands and therefore determine their excitation energy and spin parity, as well as lifetime measurements to deduce the quadrupole moments are highly desired to get a more detailed understanding of this interesting region of triaxial shapes in nuclei.

ACKNOWLEDGMENTS

This work was supported by the DST, India, under Project SR/S2/HEP-09/2005 and the UGC-DRS Programme of the Department of Physics, University of Calcutta, the German BMBF under Contract 06 BN 109.

[1] C. M. Petrache *et al.*, Phys. Rev. C **61**, 011305(R) (1999).
[2] C. M. Petrache *et al.*, Phys. Rev. C **72**, 064318 (2005).
[3] S. Lunardi *et al.*, Phys. Rev. C **69**, 054302 (2004).
[4] A. Neußer *et al.*, Phys. Rev. C **70**, 064315 (2004).
[5] C. M. Petrache *et al.* Nucl. Phys. A **617** 228 (1997).
[6] F. Brandolini *et al.*, Phys. Lett. B **388**, 468 (1996).
[7] R. Raut *et al.*, Phys. Rev. C **73**, 044305 (2006).
[8] Y. Zheng *et al.*, J. Phys. G **30**, 465 (2004).
[9] F. R. Espinoza-Quinones *et al.*, Phys. Rev. C **60**, 054304 (1999).
[10] M. Sferrazza, M. A. Cardona, D. Bazzacco, S. Lunardi, E. Maglione, and G. de Angelis, Z. Phys. A **354**, 157 (1996).
[11] Krishichayan *et al.*, Phys. Rev. C **70**, 044315 (2004).
[12] M. Sugawara *et al.*, Z. Phys. A **358**, 1 (1997).
[13] T. Rzaca-Urban *et al.*, Nucl. Phys. A **579**, 319 (1994).
[14] A. Gizon, J. Gizon, R. M. Diamond, and F. S. Stephens, J. Phys. G **4**, L171 (1978).
[15] M. Müller-Veggian, H. Beuscher, D. R. Haenni, R. M. Lieder, A. Neskakis, and C. Mayer-Böricke, Nucl. Phys. A **344**, 89 (1980).
[16] S. Kumar, R. Palit, H. C. Jain, I. Mazumdar, P. K. Joshi, S. Roy, A. Y. Deo, Z. Naik, S. S. Malik, and A. K. Jain, Phys. Rev. C **76**, 014306 (2007).
[17] Q. Xu *et al.*, Phys. Rev. C **78**, 034310 (2008).
[18] J. Simpson, Z. Phys. A **358**, 139 (1997).
[19] D. C. Radford, Nucl. Instrum. Methods A **361**, 297 (1995).
[20] J. Ludziejewski and H. Arnold, Z. Phys. A **281**, 287 (1977).
[21] M. Ferraton *et al.*, Eur. Phys. J. A **35**, 167 (2008).
[22] M. Leino, Nucl. Instrum. Methods B **126**, 320 (1997).
[23] C. Petrache (private communication).
[24] C. M. Petrache *et al.*, Phys. Lett. B **373**, 275 (1996).
[25] T. Bengtsson and I. Ragnarsson, Nucl. Phys. A **436**, 14 (1985).
[26] A. V. Afanasjev, D. B. Fossan, G. J. Lane, and I. Ragnarsson, Phys. Rep. **322**, 1 (1999).
[27] A. V. Afanasjev and I. Ragnarsson, Nucl. Phys. A **608**, 176 (1996).
[28] I. Ragnarsson, Nucl. Phys. A **557**, 167c (1993).
[29] B. G. Carlsson and I. Ragnarsson, Phys. Rev. C **74**, 011302(R) (2006).